

Dark matter self-interactions from the internal dynamics of dwarf spheroidals

Mauro Valli¹ and Hai-Bo Yu²

Dwarf spheroidal galaxies provide well-known challenges to the standard cold and collisionless dark matter scenario [1, 2]: The *too-big-to-fail* problem, namely the mismatch between the observed mass enclosed within the half-light radius of dwarf spheroidals [3, 4] and cold dark matter N-body predictions [5, 6]; The hints for inner constant-density cores [7–10]. While these controversies may be alleviated by baryonic physics and environmental effects [11–15], revisiting the standard lore of cold and collisionless dark matter remains an intriguing possibility. Self-interacting dark matter [16, 17] may be the successful proposal to such a small-scale crisis [18, 19]. Self-interactions correlate dark matter and baryon distributions, allowing for constant-density cores in low surface brightness galaxies [20–23]. Here we report the first data-driven study of the *too-big-to-fail* of Milky Way dwarf spheroidals within the self-interacting dark matter paradigm. We find good description of stellar kinematics and compatibility with the concentration-mass relation from the pure cold dark matter simulation in [24]. Within the latter, a subset of Milky Way dwarfs are well fitted by cross sections of 0.5–3 cm²/g, while others point to values greater than 10 cm²/g.

The internal dynamics of dwarf spheroidal galaxies (dSphs) of the Milky Way (MW) is commonly studied exploiting the kinematics of a stellar population of density ρ_* , in dynamical equilibrium under the gravitational potential governed by dark matter (DM), Φ_{DM} . For a spherically symmetric steady-state system, the first moment of the collisionless Boltzmann equation for the stellar phase-space distribution takes the form:

$$(\rho_* \sigma_r^2)' + 2\beta(r) \rho_*(r) \sigma_r^2(r) = -\rho_*(r) \Phi_{\text{DM}}' , \quad (1)$$

where the prime denotes logarithmic derivative in r . The stellar orbital anisotropy, $\beta \equiv 1 - \sigma_t^2/\sigma_r^2$, measures the deviation from isotropy in the stellar velocity dispersion tensor. Photometric observations of the surface brightness of these systems constrain ρ_* . Supplying

equation (1) with Poisson's equation, mass $M(r)$ and orbital anisotropy $\beta(r)$ are inferred from line-of-sight projected spectroscopic measurements, see e.g. [25], leading in general to a degeneracy problem.

The self-interacting dark matter (SIDM) paradigm can be investigated with equation (1) by means of a semi-analytical halo model based on simple physical grounds. Introducing the DM self-scattering rate as $\Gamma \equiv \langle \sigma v \rangle \rho / m$, with velocity averaged cross section, $\langle \sigma v \rangle$, density ρ , and particle mass m , we can define the scale r_1 at which $\Gamma|_{r_1} \simeq t_{\text{age}}^{-1}$, with t_{age} the typical age of the system. As illustrated in [17, 20], r_1 sets a transition from the regime of an isothermal gas with pressure $p \propto \rho$ ($r \lesssim r_1$) to the one of a non-interacting particle ensemble ($r \gtrsim r_1$). For DM dominated systems as MW dSphs, in the inner halo region the SIDM profile is given by:

$$x \ddot{h} + 2\dot{h} = -x \exp(h(x)) , \quad \lim_{x \rightarrow 0} h(x) = 0 , \quad \lim_{x \rightarrow 0} \dot{h} = 0 , \quad (2)$$

where upper-dots denote derivatives in x , where we introduced $x \equiv \sqrt{4\pi G_N \rho_0} r / \sigma_0$ with G_N the gravitational constant, and $h \equiv \ln(\rho/\rho_0)$. The physical halo from equation (2) is an isothermal cored profile involving the one-dimensional DM velocity dispersion, σ_0 , defining the SIDM isothermal gas law, and the central density, ρ_0 . The solution of equation (2) is then matched at r_1 to the Navarro-Frenk-White (NFW) model [26]. The condition of continuity of mass and density at r_1 implies:

$$\left(\frac{1 + x_{s1}}{x_{s1}} \right)^2 \left(\log(1 + x_{s1}) - \frac{x_{s1}}{1 + x_{s1}} \right) = \mathcal{R}|_{r_1} , \quad (3)$$

with $x_{s1} \equiv r_s/r_1$, r_s denoting NFW scale radius, and \mathcal{R} being the SIDM ratio $M(r)/(4\pi r^3 \rho(r))$. Equation (3) gives a viable matching if $\mathcal{R}|_{r_1} > 0.5$, which ensures $x_{s1} > 0$. The NFW normalization can be simply read as $\rho_s = x_{s1}(1 + x_{s1})^2 \rho(r_1)$.

At given r_1 , we can also estimate the self-scattering cross section per unit mass of DM particles. This is obtained exploiting the condition $\Gamma|_{r_1} \simeq t_{\text{age}}^{-1}$, yielding:

$$\sigma/m \simeq \sqrt{\pi} / (4\sigma_0 \rho(r_1) t_{\text{age}}) , \quad (4)$$

where $\sigma \simeq \langle \sigma v \rangle / \langle v \rangle$ and $\langle v \rangle$ is expected to follow a Maxwellian distribution according to the thermalized inner halo by DM self-interactions within r_1 [17, 20].

Using equation (1) and such semi-analytical halo model [17, 20] – well-tested against SIDM simulations – we undertake a minimal approach to SIDM paradigm and explore its

predictions for the stellar kinematics in MW dSphs. We focus on the eight brightest MW satellites – the classical dSphs – regarded as relaxed systems, with small ellipticities [25]. They represent the baseline of the too-big-to-fail (TBTf) problem [5, 6]. We perform fits to the spectroscopic dataset of classical dSphs, adopting a standard Gaussian test statistic. Details about our fitting procedure are given in **Methods**.

Main goal of our study is to assess to which extent TBTf in MW dSphs can be ameliorated within the SIDM scenario. Then, together with the observational information from the stellar kinematics, we also take into account the predictions of pure cold dark matter (CDM) simulations. We specifically exploit here the recent outcome obtained in the N-body study of [24], from where we extract the concentration-mass relation:

$$\log_{10} \left(\frac{R_{\max}}{\text{kpc}} \right) = 0.48 + 0.18 \log_{10} \left(\frac{V_{\max}}{\text{km/s}} \right) , \quad (5)$$

within a NFW model with maximum circular velocity V_{\max} and corresponding scale radius R_{\max} . In the whole work, we assume equation (5) to be a reliable proxy for the CDM-only gravitational potential in MW dSphs, assigning 0.2 dex scatter on R_{\max} for $V_{\max} \sim 25\text{--}55$ km/s, see **Methods** for further details.

To start with, we report in figure 1 the best-fit result obtained considering only the stellar kinematic data of MW dSphs, i.e. without imposing the constraint appearing in equation (5). We model the stellar orbital anisotropy as constant, $\beta(r) = \beta_c$, and consider a cuspy DM halo (orange dotted line) and a cored one (green dotted line), respectively described by NFW and Burkert [27] profiles. Both cases provide a good fit of dSph stellar kinematics. This result shows that both cuspy and cored DM halos can yield *a priori* an optimal description of the kinematic dataset here considered in virtue of the mass-anisotropy degeneracy pertaining to equation (1).

However, if we now focus on the case of cuspy halo profiles and introduce in the fit the constraint from equation (5), i.e. we restrict to the representative outcome of pure CDM simulations as in [24], an overall satisfactory description of dSph spectroscopic data is no longer available. In figure 1 the dot-dashed black line captures this failure representing the NFW scenario subject to the concentration-mass relation with relative scatter as extracted from [24]. Most importantly, this fit is performed including also a more general and realistic orbital anisotropy modeling, namely [28]:

$$\beta(r) = (\beta_0 + \beta_{\infty}(r/r_{\beta})^{\eta}) / (1 + (r/r_{\beta})^{\eta}) , \quad (6)$$

i.e. a spatial interpolation of the regime of stellar motion at the centre, controlled by β_0 , and towards the outer region, regulated by β_∞ , with characteristic scale r_β and slope η . The data overshooting in several analyzed objects constitutes the essence of the TBTF problem emerging within the CDM picture.

Finally, in the same figure we present the best-fit results for the SIDM scenario. Blue curves correspond to the case where we perform the SIDM fit varying a total of seven parameters, implementing equation (6) together with the 3-parameter semi-analytical halo model, while the dashed light-blue one represents the same SIDM halo model assuming constant stellar anisotropy. We observe that radial dependence in the stellar orbital anisotropy profile is needed in order to find an overall good fit of dSph kinematics: The general trend for the best-fit anisotropy corresponds to a sharp ($\eta \gtrsim 5$) transition from $\beta_0 \simeq 0$ to $\beta_\infty \simeq 1$ at r_β , close to the stellar half-light radius. The only exception to this behaviour is provided by Sextans, where circular-like orbits are preferred in the outer region as a consequence of requiring $r_1 \lesssim 30$ kpc (see **Methods**). The underlying NFW profile follows the $R_{\text{max}} - V_{\text{max}}$ scatter in the concentration-mass relation given in equation (5), obtained from [24]. CDM-only predictions are recovered above r_1 , highlighted in figure 1. Therefore, the SIDM paradigm seems to offer a viable proposal for the solution of the TBTF puzzle.

The 7-parameter SIDM fit can be compared against the 6-parameter NFW one – both subject to the constraint from [24] – by means of the Akaike Information Criterion (A.I.C.), whose definition is recalled in **Methods**. In figure 1 we report differences $\Delta\text{A.I.C.} = \text{A.I.C.}_{\text{SIDM}} - \text{A.I.C.}_{\text{CDM}}$: Model selection follows according to the smallest possible A.I.C. value. Large differences $\Delta\text{A.I.C.} < 0$ are found for four of the eight MW classics, showing that stellar kinematics and the N-body input of pure CDM simulations combined together yield a net preference for the SIDM paradigm.

In light of the promising outcome for SIDM resulting from the inspection of the best-fit cases in figure 1, we continue our study performing a Bayesian analysis of the 7-parameter SIDM model in order to carefully assess the uncertainties on the estimated model parameters through the evaluation of their posterior probability density function (p.d.f.). Following equation (4), we eventually aim to marginalize over nuisance parameters in order to derive the first data-driven estimate in literature of the self-scattering cross section of DM particles in MW dSphs. Details on the Markov chain Monte Carlo (MCMC) analysis performed for the Bayesian fit of the SIDM model are reported in **Methods**.

In table I we collect for each dSph the mode and the 68% highest posterior density (h.p.d.) interval of the marginalized distribution for the fitted parameters. The SIDM best-fit in figure 1 approximately lies within 68% h.p.d. of parameters posterior. From the estimated values for r_β , we highlight Sculptor, Sextans and Fornax to be the most representative cases of relevance for spatially dependence in the stellar orbital anisotropy profile.

Using the MCMC events for the estimated SIDM parameters σ_0 , ρ_0 and r_1 and marginalizing over orbital anisotropy ones, we can derive the posterior p.d.f. for r_s and ρ_s of the matched NFW profile at r_1 by means of equation (3). Eventually, we compute the posterior distribution for the SIDM circular velocity profile $V_c(r) = \sqrt{G_N M(r)/r}$ at a given radius r . In figure 2, we show the typical spread on the SIDM circular velocity profile for each dSph within the 10-th and 90-th percentile of V_c posterior p.d.f. at different radii. In the outer region, we highlight the expected agreement with the CDM-only output from [24], represented by the gray band. In the inner region, we find satisfactory match to dSph half-light masses originally proposed in [4]: Colored squares represent nominal values for $V_c(r_{1/2}) \simeq \sqrt{3 \langle \sigma_{los}^2 \rangle}$, here re-estimated as detailed in **Methods**. Figure 2 reinforces the idea that the SIDM proposal can be a promising solution to the TBTF problem. Figure 1 and figure 2 together offer an original detailed inspection of the TBTF puzzle.

We eventually utilize the condition $\Gamma|_{r_1} \simeq t_{\text{age}}^{-1}$ to provide a data-driven estimate of the SIDM cross section. Practically, we need to marginalize over dSph age: We assume t_{age} to be flatly distributed in the range 8–12 Gyr, motivated by the observational indicators pointing MW dSphs to be early-type galaxies [25]. We collect our estimate of the averaged cross section per unit mass and particle velocity in the last two columns of table I. Notably, while the probed range of averaged velocities turns out to be relatively similar among MW classics, spanning ~ 30 – 70 km/s within 68% h.p.d., the velocity averaged SIDM cross section covers three orders of magnitude. In figure 3 we zoom on this aspect directly investigating the posterior distribution of the DM self-scattering cross section per unit mass, equation (4). We find Ursa Minor, Draco, Leo I, and Leo II consistently probing cross sections ~ 0.1 – 1.0 $\text{cm}^2 \text{g}^{-1}$ within 68% h.p.d.. We also observe Sextans and Fornax to be sensitive to very large cross-section values, with σ/m posterior p.d.f. peaked around ~ 20 and 40 $\text{cm}^2 \text{g}^{-1}$ respectively. Sculptor and Carina sit in between the two groups, with the former pointing to $\mathcal{O}(1)$ $\text{cm}^2 \text{g}^{-1}$, while the latter sharing good overlap with Sextans in σ/m posterior p.d.f..

The result depicted in figure 3 can be summarized as follows: Within the SIDM model

respecting the scatter of the concentration-mass relation read out from the pure CDM simulation presented in [24], a *diversity* in the DM particle cross section probed by MW dSphs is strictly demanded by the measured stellar kinematics. Looking at 68% h.p.d., five of the classical dSphs probe particle cross section well consistent with $\sigma/m \sim 0.5\text{--}3 \text{ cm}^2\text{g}^{-1}$, an interval highlighted in [17, 22] with the analysis of several low-surface brightness and spiral dwarf galaxies within the same SIDM halo model here considered. However, Carina, Sextans and Fornax limit this qualitative interpretation towards a consistent SIDM picture, with Sextans already ruling out $\sigma/m \leq 3 \text{ cm}^2\text{g}^{-1}$ within 99.7% h.p.d.. We remark that figure 3 provides a cross-section hierarchy that matches the benchmark trends found in previous SIDM-only simulations [21, 24, 29], while encoding for the first time the associated observational error for each of the galaxies. We highlight two plausible explanations to the inferred hierarchy in the cross section. First, environmental effects such as tidal stripping due to the MW baryonic disc could be important [30] for these systems, e.g. increasing the scatter of the concentration-mass relation adopted in this work. Interestingly, a TBTF puzzle has been found for dwarf galaxies in the field [31, 32], where the environmental effects are absent. It would be of great interest to apply the same minimal approach to scrutinize the TBTF problem in field dwarfs and see whether their stellar kinematics also prefer a diverse range of σ/m . Second, the presence of very light degrees of freedom in the SIDM model may lead to the matter-power suppression that modifies the concentration-mass relation given in equation (5), see [24], and the extent to which it may work remains to be investigated in detail. Our present study with a minimal approach for SIDM provides a baseline for the assessment of these effects, which we leave for future investigation.

-
- [1] Tulin, S. & Yu, H.-B. Dark Matter Self-interactions and Small Scale Structure. *Phys. Rep.* **730**, 1-57 (2018).
 - [2] Bullock, J. S. & Boylan-Kolchin, M. Small-Scale Challenges to the Λ CDM Paradigm. *Annu. Rev. Astron. Astr.* **55**, 343-387 (2017).
 - [3] Walker, M. G., *et al.* A Universal Mass Profile for Dwarf Spheroidal Galaxies?. *Astrophys. J.* **704**, 1274-1287 (2009).
 - [4] Wolf, J., *et al.* Accurate masses for dispersion-supported galaxies. *Mon. Not. R. Astron. Soc.*

- 406, 1220-1237 (2010).
- [5] Boylan-Kolchin, M., Bullock, J. S. & Kaplinghat, M. Too big to fail? The puzzling darkness of massive Milky Way subhaloes. *Mon. Not. R. Astron. Soc.* **415**, L40-L44 (2011).
 - [6] Boylan-Kolchin, M., Bullock, J. S. & Kaplinghat, M. The Milky Way's bright satellites as an apparent failure of Λ CDM. *Mon. Not. R. Astron. Soc.* **422**, 1203-1218 (2012).
 - [7] Battaglia, G., *et al.* The kinematic status and mass content of the Sculptor dwarf spheroidal galaxy. *Astrophys. J.* **681**, L13 (2008).
 - [8] Amorisco, N. C. & Evans, N. W. Dark Matter Cores and Cusps: The Case of Multiple Stellar Populations in Dwarf Spheroidals. *Mon. Not. R. Astron. Soc.* **419**, 184-196 (2012).
 - [9] Walker, M. G. & Peñarrubia, J. A Method for Measuring (Slopes of) the Mass Profiles of Dwarf Spheroidal Galaxies. *Astrophys. J.* **742**, 20 (2011).
 - [10] Strigari, L. E., Frenk, C. S. & White, S. D. M. Dynamical models for the Sculptor dwarf spheroidal in a Λ CDM universe. *Astrophys. J.* **838**, 123 (2017).
 - [11] Pontzen, A. & Governato, F. Cold dark matter heats up. *Nature* **506**, 171-178 (2014).
 - [12] Sawala, T., *et al.* The APOSTLE simulations: solutions to the Local Group's cosmic puzzles. *Mon. Not. R. Astron. Soc.* **457**, 1931-1943 (2016).
 - [13] Dutton, A. A., *et al.* NIHAO V: too big does not fail - reconciling the conflict between Λ CDM predictions and the circular velocities of nearby field galaxies. *Mon. Not. R. Astron. Soc.* **457**, L74-L78 (2016).
 - [14] Wetzel, A. R., *et al.* Reconciling dwarf galaxies with Λ CDM cosmology: Simulating a realistic population of satellites around a Milky Way-mass galaxy. *Astrophys. J. Lett.* **827** L23 (2016).
 - [15] Fattahi, A., *et al.* The cold dark matter content of Galactic dwarf spheroidals: no cores, no failures, no problem. *ArXiv e-prints* (2016), 1607.06479.
 - [16] Spergel, D. N. & Steinhardt, P. J. Observational evidence for self-interacting cold dark matter. *Phys. Rev. Lett.* **84**, 3760-3763 (2000).
 - [17] Kaplinghat, M., Tulin, S., & Yu, H.-B. Dark Matter Halos as Particle Colliders: A Unified Solution to Small-Scale Structure Puzzles from Dwarfs to Clusters. *Phys. Rev. Lett.* **116**, 041302 (2016).
 - [18] Vogelsberger, M., Zavala, J. & Loeb, A. Subhaloes in Self-Interacting Galactic Dark Matter Haloes. *Mon. Not. R. Astron. Soc.* **423**, 3740-3752 (2012).
 - [19] Rocha, M., *et al.* Cosmological Simulations with Self-Interacting Dark Matter I: Constant

- Density Cores and Substructure. *Mon. Not. R. Astron. Soc.* **430**, 81-104 (2013).
- [20] Kaplinghat, M., Keeley, R. E., Linden, T., & Yu, H.-B. Tying Dark Matter to Baryons with Self-interactions. *Phys. Rev. Lett.* **113**, 021302 (2014).
 - [21] Elbert, O. D., *et al.* Core Formation in Dwarf Halos with Self Interacting Dark Matter: No Fine-Tuning Necessary. *Mon. Not. R. Astron. Soc.* **453**, 29-37 (2015).
 - [22] Kamada, A., Kaplinghat, M., Pace, A. B., & Yu, H.-B. How the Self-Interacting Dark Matter Model Explains the Diverse Galactic Rotation Curves. *Phys. Rev. Lett.* **119**, 111102 (2017).
 - [23] Creasey, P., *et al.* Spreading out and staying sharp - Creating diverse rotation curves via baryonic and self-interaction effects. *Mon. Not. R. Astron. Soc.* **468**, 2283 (2017).
 - [24] Vogelsberger, M., *et al.* ETHOS - An Effective Theory of Structure Formation: Dark matter physics as a possible explanation of the small-scale CDM problems. *Mon. Not. R. Astron. Soc.* **460**, 1399-1416 (2016).
 - [25] Battaglia, G., Helmi, A. & Breddels, M. Internal kinematics and dynamical models of dwarf spheroidal galaxies around the Milky Way. *New Astron. Rev.* **57**, 52-59 (2013).
 - [26] Navarro, J. F., Frenk, C. S., & White S. D. M. A Universal Density Profile from Hierarchical Clustering. *Astrophys. J.* **490**, 493-508 (1997).
 - [27] Burkert, A. The Structure of Dark Matter Halos in Dwarf Galaxies. *Astrophys. J.* **447**, L25 (1995).
 - [28] Baes, M. & Van Hese, E. Dynamical models with a general anisotropy profile. *Astron. Astrophys.* **471**, 419-432 (2007).
 - [29] Zavala, J., Vogelsberger M., & Walker, M. G. Constraining Self-Interacting Dark Matter with the Milky Way's dwarf spheroidals. *Mon. Not. R. Astron. Soc.* **431**, L20-L24 (2013).
 - [30] J. Peñarrubia, *et al.*, The impact of dark matter cusps and cores on the satellite galaxy population around spiral galaxies. *Mon. Not. R. Astron. Soc.* **406**, 1290-1305 (2010).
 - [31] Garrison-Kimmel, S., Boylan-Kolchin, M., Bullock, J. S. & Kirby, E. N. Too Big to Fail in the Local Group. *Mon. Not. R. Astron. Soc.* **444**, 222-236 (2014).
 - [32] Papastergis, E., Giovanelli, R., Haynes M. P. & Shankar F. Is there a “too big to fail” problem in the field?. *Astron. Astrophys.* **574**, A113 (2015)

Correspondence: M.V. is in charge for any enquiry on the work and requests for materials (email: mauro.valli@roma1.infn.it).

Acknowledgments: M.V. acknowledges support from the European Research Council under the European Union’s Seventh Framework Programme (FP/2007-2013) / ERC Grant Agreements n. 279972 “NPFlavour”. H.B.Y. acknowledges support from U. S. Department of Energy under Grant No. de-sc0008541 and the Hellman Fellows Fund. M.V. and H.B.Y. are grateful to Matthew Walker for the binned kinematic dataset adopted in the analysis, acknowledge Peter Creasey, Manoj Kaplinghat, Mihael Petač, Laura Sales and Piero Ullio for useful discussions, thank organizers and participants of the stimulating workshops “Self-Interacting Dark Matter” (Niels Bohr Institute), “WIMPs vs non-WIMPs in dwarf spheroidal galaxies” (University of Turin).

Author Contributions: M.V. performed the required analytical computations and numerical analysis. The original idea of the study is attributed to H.B.Y., who supervised the work. Both M.V. and H.B.Y. contributed to the writing of the manuscript.

Author Information:

¹*INFN, Sezione di Roma, P.le A. Moro 2, I-00185 Roma, Italy*

²*Department of Physics and Astronomy, University of California, Riverside, California 92521, USA*

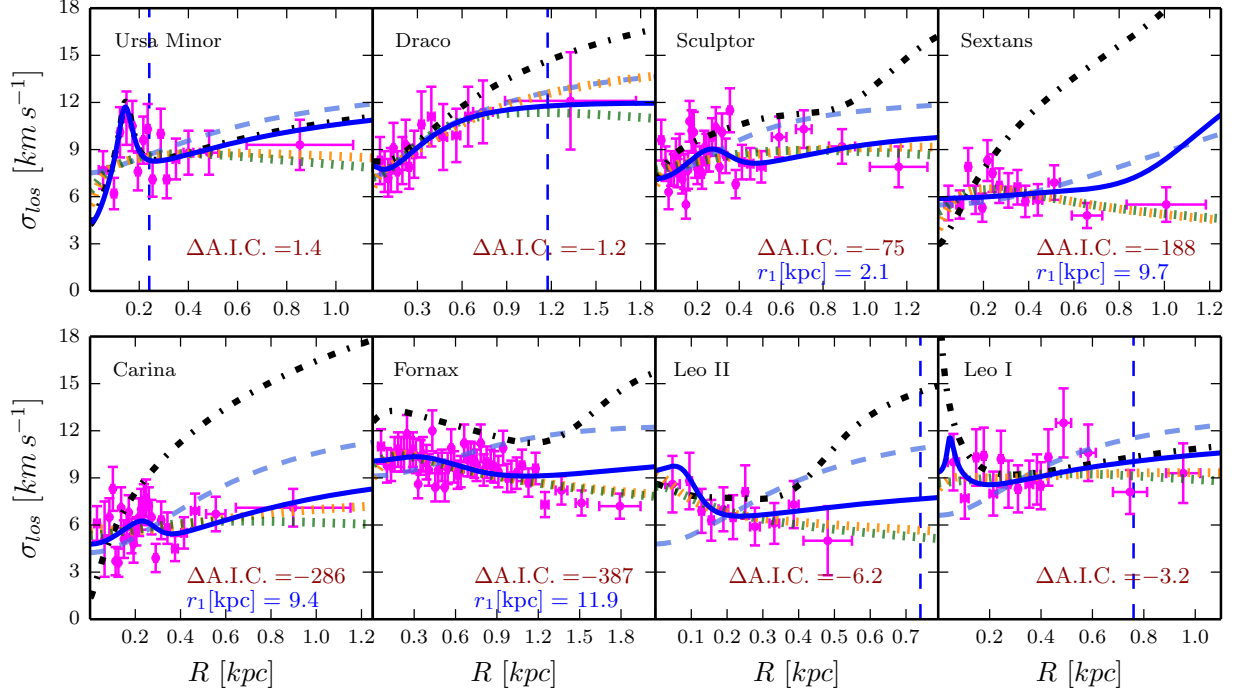


FIG. 1. *Line-of-sight velocity dispersion profiles for the classical dwarf satellites from the joint fit of the stellar kinematics and the CDM concentration-mass relation.* In magenta, the stellar kinematic dataset analyzed in the present study: We show binned line-of-sight velocity dispersions, see e.g. [3], together with standard deviation and spatial bin width. Dashed light-blue curves refer to the best-fit SIDM scenario with spatially constant stellar anisotropy. Blue and dot-dashed black lines correspond respectively to the SIDM (7 parameters) and CDM best-fit (6 parameters) cases using the orbital anisotropy function of equation (6). Transition from core to cusp in SIDM is highlighted by vertical dashed line or reported r_1 best-fit value. Differences in the Akaike Information Criterion (A.I.C.) are reported between the two cases: $\Delta\text{A.I.C.} \ll 0$ highlights SIDM as the preferred model. Green and orange dotted lines are also reported for the fit of cored and cuspy DM halo profiles without imposing the concentration-mass relation.

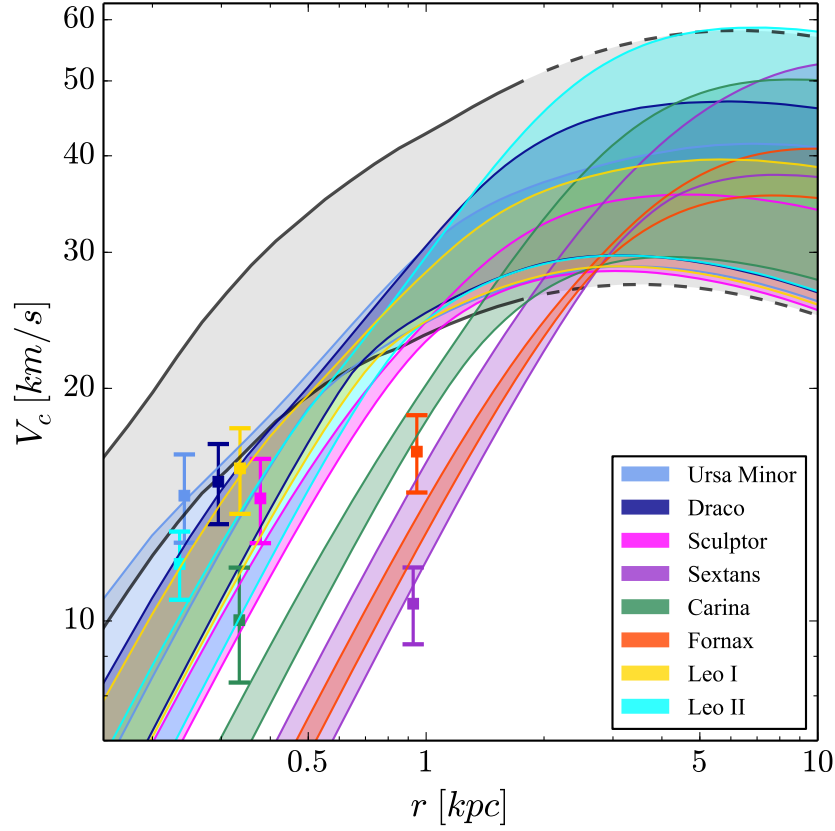


FIG. 2. *Circular velocity profiles obtained from the Bayesian analysis of the 7-parameter SIDM model.* Colored band for each dwarf includes the 10-th and 90-th percentile of V_c posterior distribution. Colored points indicate dSph mass estimator at half-light radius, see e.g. [4], with related uncertainty as inferred in [15]. Gray band encompasses the most-massive 15 subhalos from CDM-only simulation of [24], and it is extrapolated here above ~ 2 kpc with the NFW model (dashed lines).

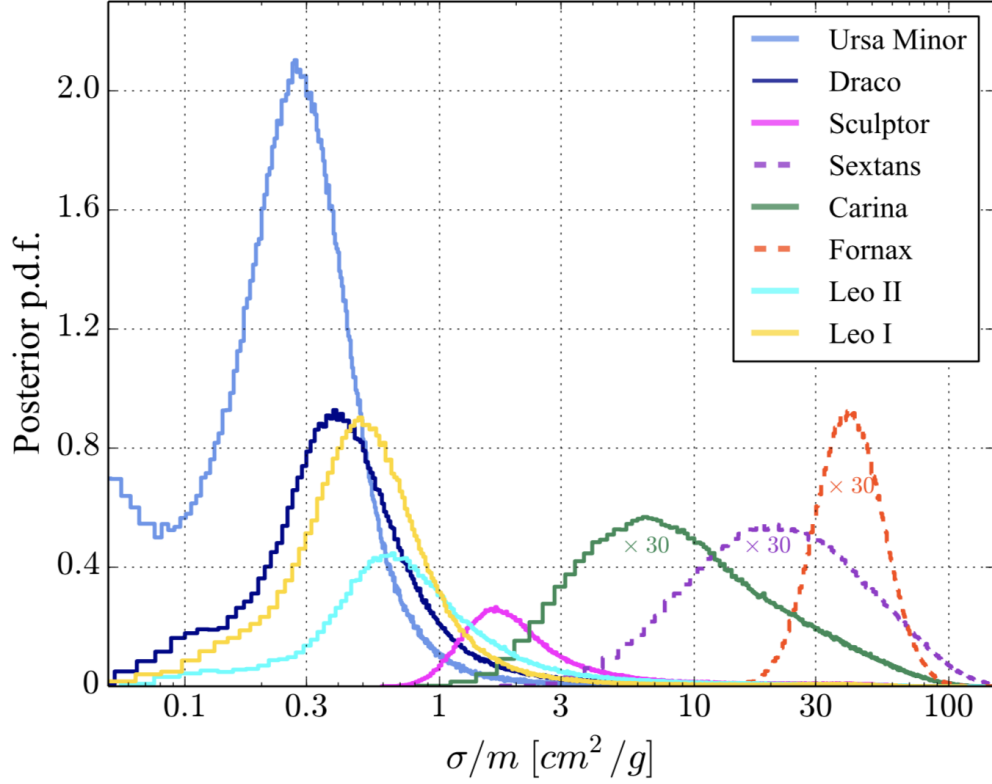


FIG. 3. *Posterior probability density function (p.d.f.) for the SIDM cross section probed by classical dwarf spheroidals according to the concentration-mass relation from [24]. For the sake of readability, histograms for Sextans, Carina and Fornax are normalized to an area equal to 30 times unity. Note that if both Fornax and Sextans are hosted by subhalos less-massive than the 15 ones characterizing the spread of the gray band in figure 2, see also [24], a smaller σ/m may be consistent with dSph stellar kinematics [29].*

TABLE I. *Estimated parameters and velocity averaged cross section for the SIDM model. Mode and 68% highest density interval of the posterior distribution of SIDM parameters, σ_0 [km/s], ρ_0 [$10^7 M_\odot/\text{kpc}^3$], r_1 [kpc], and of orbital anisotropy ones, r_β [kpc], η , β_0 , β_∞ . Same statistics is also reported for the SIDM averaged self-scattering cross section per unit mass, $\langle\sigma v\rangle/m$ [$\text{cm}^3/(s g)$], and velocity, $\langle v\rangle$ [km/s].*

<i>dSph</i>	σ_0	ρ_0	r_1	r_β	η	β_0	β_∞	$\langle\sigma v\rangle/m$	$\langle v\rangle$
Ursa Minor	$15.0^{+6.0}_{-2.4}$	$11.9^{+9.3}_{-3.3}$	$0.43^{+0.66}_{-0.41}$	$1.08^{+0.62}_{-1.05} \times 10^{-1}$	$9.9^{+0.1}_{-5.2}$	$-0.2^{+0.2}_{-24} \times 10^{-1}$	$0.77^{+0.09}_{-0.22}$	$9.4^{+16}_{-9.2}$	$33.8^{+14}_{-5.5}$
Draco	$19.7^{+5.5}_{-4.3}$	$8.8^{+4.4}_{-1.9}$	$0.9^{+3.9}_{-0.8}$	$3.0^{+5.3}_{-0.0} \times 10^{-3}$	$6.7^{+0.4}_{-5.6}$	$-0.2^{+0.2}_{-16} \times 10^{-1}$	$0.54^{+0.20}_{-0.25}$	34^{+450}_{-6}	$44.4^{+12}_{-9.7}$
Sculptor	$18.4^{+2.1}_{-0.9}$	$6.1^{+0.6}_{-1.0}$	$1.7^{+3.5}_{-0.3}$	$1.7^{+3.5}_{-0.3}$	$1.6^{+5.1}_{-0.4}$	$-0.2^{+0.2}_{-19} \times 10^{-2}$	$0.80^{+0.06}_{-0.10}$	67^{+740}_{-34}	$41.5^{+4.8}_{-2.0}$
Sextans	$27.8^{+4.2}_{-3.6}$	$1.14^{+0.28}_{-0.32}$	$11.0^{+5.2}_{-3.4}$	$1.34^{+0.37}_{-0.41}$	$9.9^{+0.1}_{-3.3}$	$-0.1^{+0.01}_{-9.3} \times 10^{-2}$	$0.0^{+0.0}_{-10}$	1442^{+2002}_{-938}	$62.8^{+9.5}_{-8.1}$
Carina	$21.3^{+3.9}_{-3.6}$	$2.56^{+0.46}_{-0.35}$	$4.0^{+4.8}_{-0.6}$	$3.0^{+72}_{-0.0} \times 10^{-3}$	$1.7^{+5.3}_{-0.7}$	$-0.1^{+0.1}_{-16} \times 10^{-1}$	$0.70^{+0.13}_{-0.08}$	315^{+1311}_{-175}	$48.2^{+8.7}_{-8.2}$
Fornax	$23.9^{+1.2}_{-1.3}$	$1.11^{+0.12}_{-0.08}$	$10.9^{+1.4}_{-1.7}$	$0.56^{+0.01}_{-0.20}$	$2.74^{+0.89}_{-0.56}$	$-0.1^{+0.1}_{-3.2} \times 10^{-1}$	$0.89^{+0.03}_{-0.03}$	2116^{+861}_{-567}	$54.0^{+2.8}_{-3.0}$
Leo II	$18.5^{+8.3}_{-2.4}$	$6.3^{+2.8}_{-1.3}$	$1.2^{+5.2}_{-0.6}$	$3.0^{+45}_{-0.0} \times 10^{-3}$	$9.9^{+0.1}_{-5.6}$	$0.0^{+0.0}_{-2.3}$	$0.81^{+0.07}_{-0.10}$	25^{+677}_{-24}	$41.8^{+19}_{-5.4}$
Leo I	$18.8^{+2.8}_{-3.2}$	$8.5^{+3.9}_{-1.9}$	$1.0^{+1.9}_{-0.8}$	$3.0^{+4.6}_{-0.0} \times 10^{-3}$	$9.8^{+0.2}_{-8.4}$	$-0.1^{+0.1}_{-20} \times 10^{-1}$	$0.73^{+0.10}_{-0.17}$	18^{+142}_{-17}	$42.3^{+6.2}_{-7.2}$

Methods

Spherical Jeans analysis. In this work we analyze the stellar kinematic dataset for the classical dSphs presented in [33], applying the standard Jeans analysis under spherical approximation. We solve equation (1) for σ_r and project it along the line-of-sight in order to connect it to observations according to (see, e.g., [25]):

$$P_{los}(R) = \int_R^\infty \frac{dr^2}{\sqrt{r^2 - R^2}} \left(1 - \beta(r) \frac{R^2}{r^2} \right) p_r(r), \quad (7)$$

where $p_r \equiv \rho_\star \sigma_r^2$, $P_{los} \equiv \Sigma_\star \sigma_{los}^2$. The surface brightness, Σ_\star , is obtained from the stellar density, ρ_\star , via an Abel transform in r^2 ; the dimensional factor between the two gets simplified when combining the solution of equation (1) with the expression in equation (7). In our study the description of the stellar profile, ρ_\star , is given in terms of the Plummer model [34]. We adopt the heliocentric distances of the MW satellites and the projected half-light radii reported in [35] (table 2 and 3 of the reference).

As already outlined in the main text, for the stellar anisotropy profile, $\beta(r)$, we consider both the simple ansatz of a spatially constant orbital anisotropy and the more general functional form given in equation (6). In the spherical Jeans analysis, a generic parametrization of the stellar anisotropy may be indeed recommended in virtue of the mass-anisotropy degeneracy and the possible bias also stemming from the modeling of ρ_\star [36]. Note that the solution of the Jeans equation does not guarantee on general grounds a physical phase-space distribution function. In order to meet the known criteria for non-negative phase-space distributions, in our analysis we restrict $\beta(r=0) \leq 0$ according to the result in [37] and assume $r_\beta \gtrsim 1$ pc, since radial anisotropy close to the center of the system may underly unphysical phase-space densities [38]. Moreover, the adopted binned kinematic dataset does not probe smaller scales. For what concerns the outer region of the system, we actually assume that the DM halo of the classical satellites can be extended up to $\mathcal{O}(10)$ kpc. Such order of magnitude estimate may be easily obtained from the Roche limit of satellite galaxies under the influence of the MW gravitational field [39]:

$$r_t = \left(\frac{G_N}{2} \frac{M_{\text{dSph}}}{M_{\text{MW}}} \left(\frac{d}{\sigma_{\text{MW}}} \right)^2 \right)^{\frac{1}{3}} \sim 10 \text{ kpc}, \quad (8)$$

where $M_{\text{dSph}}/M_{\text{MW}} \sim 10^{-3}$ is the typical ratio of the virial mass estimates for dSph subhalo and the MW-sized host halo, $\sigma_{\text{MW}} \sim 200$ km/s being MW velocity dispersion in the satellite rest frame, $d \sim 100$ kpc the distance between the two systems.

It is important to remark that the precise value of r_t does not really impact the result of our numerical analysis of the SIDM model as long as $r_1 < r_t$. This condition is indeed at the basis of the matching to the outer NFW profile as described in detail in the text for the SIDM scenario. Looking at table I, Sextans is the only object that requires r_t as large as ~ 15 kpc in order to satisfy the condition $r_1 < r_t$ within 68% h.p.d. interval for r_1 . More generally, in our Bayesian fit all the eight marginalized distributions related to r_1 are well-determined within the range of the adopted prior, in particular $r_1 \leq 30$ kpc.

Finally, we note that the spherical Jeans equation (1), combined with Poisson’s equation, can be inspected in order to motivate the existence of a mass estimator at the half-light radius, namely $M(r_{1/2}) \simeq 3 r_{1/2} \langle \sigma_{\text{los}}^2 \rangle / G_N$ [4], where $\langle \sigma_{\text{los}}^2 \rangle$ is the luminosity average of the squared line-of-sight velocity dispersion. While such expression is in agreement with previous numerical findings [3] and recent N-body simulations [15, 40, 41], in [4, 42] some theoretical bias was highlighted for such mass estimator in relation to sharp transitions in the radial stellar motion. Following [42], data points reported in figure 2 are obtained estimating $\langle \sigma_{\text{los}}^2 \rangle$ via a fit to the stellar kinematics adopted in this work assuming a spatially constant line-of-sight velocity dispersion, $\bar{\sigma}_{\text{los}}$. A quite conservative error conform to the recent findings in [15] is then assigned to $V_c(r_{1/2}) = \sqrt{3} \bar{\sigma}_{\text{los}}$.

Concentration-mass relation for MW dSphs. The concentration-mass relation in equation (3) sits at the basis of the results presented in our analysis of the TBTF problem in MW dSphs. In order to derive it, we first of all read out the CDM band in the right panel of figure 9 of [24], comprising the circular velocity profile of the fifteen most massive subhalos hosted by a MW-like galaxy of about $10^{12} M_{\odot}$. According to the estimate given in equation (8) for the size of the DM halo in MW dSphs, we extrapolated the upper and lower curves to 10 kpc using NFW profile with $\log_{10}(V_{\text{max}}) \simeq 1.76$ km/s, $\log_{10}(R_{\text{max}}) \simeq 0.79$ kpc, and $\log_{10}(V_{\text{max}}) \simeq 1.44$ km/s, $\log_{10}(R_{\text{max}}) \simeq 0.54$ kpc, respectively. In particular, we find the median of the constructed band (the one reported in our figure 2) to be described by a NFW circular velocity with $\log_{10}(V_{\text{max}}) \simeq 1.64$ km/s, $\log_{10}(R_{\text{max}}) \simeq 0.78$ kpc. Fixing V_{max} to such a median value, and assuming a correlation on $R_{\text{max}} - V_{\text{max}}$ of the form

$\log_{10}(R_{\max}/[\text{kpc}]) = \alpha_1 + \alpha_2 \log_{10}(V_{\max}/[\text{km/s}])$, we can determine $\alpha_{1,2}$. We exploit thirty logarithmically spaced points sampled from the CDM band in figure 2. Taking into account the median and the width of the band, we estimate $\alpha_1 \simeq 0.48$, $\alpha_2 \simeq 0.18$. As a cross-check for the consistency of the derived log-scale relation for $R_{\max} - V_{\max}$, we have also calibrated the NFW profile on the CDM density profile provided in [24] (left panel of figure 9 of the reference), finding consistent $\alpha_{1,2}$ values.

Equipped with such concentration-mass relation, we can estimate the allowed spread on R_{\max} and V_{\max} according to the outcome in [24]. Varying R_{\max} for fixed values of V_{\max} , namely 25, 40, 55 km/s, we end up estimating an overall spread on R_{\max} of about 0.2 dex in order to span the whole gray band in the right panel of figure 9 in [24]. Note that, while our study of the SIDM model importantly depends on the adopted spread and functional form of the concentration-mass relation discussed here, our derivation of the latter may be regarded as “conservative”. Indeed, we are including the spread of the fifteen most massive CDM subhalos as representative of the eight most luminous MW dSph satellites analyzed in our work. Restricting to the spread reported e.g. in [29] for the classical satellites (figure 2 of the reference), would have led to a much more restrictive constraint in our analysis and would be translated into a stronger tension for CDM in our inspection of the TBTF problem. In order to stick to what illustrated in [24] within a minimal set of assumptions, we do not impose in our study a definite range on V_{\max} , but rather require $V_c(r = 0.5 \text{ kpc}) > 19 \text{ km/s}$, together with $25 \text{ km/s} < V_c(r = 10 \text{ kpc}) < 60 \text{ km/s}$, consistently with the CDM band in figure 2.

Test statistic and MCMC analysis. The statistical analysis carried out in the present work is based on the log-likelihood function: $\log \mathcal{L}_{\text{tot}} = \log \mathcal{L}_{\text{kin}} + \log \mathcal{L}_{\text{CDM}}$. The former of the two pieces is the test statistic for the analysis of the binned kinematic data reported for each of the eight classical dSphs in figure 1. For N radial bins, we adopt the following Gaussian likelihood function:

$$-2 \log \mathcal{L}_{\text{kin}} = \sum_{i=1}^N \left(\frac{\sigma_{\text{los}}^{(i)} - \sigma_{\text{los}}(R^{(i)})}{\Delta \sigma_{\text{los}}^{(i)}(R^{(i)})} \right)^2 + \log \left(2\pi \left(\Delta \sigma_{\text{los}}^{(i)}(R^{(i)}) \right)^2 \right). \quad (9)$$

The standard deviation $\Delta \sigma_{\text{los}}^{(i)}$ includes both the observational error measured for the binned line-of-sight velocity dispersions, $\delta \sigma_{\text{los}}^{(i)}$, and the error associated to the width of the radial bin:

$$\Delta \sigma_{\text{los}}^{(i)} \equiv \sqrt{\left(\delta \sigma_{\text{los}}^{(i)} \right)^2 + \frac{1}{4} \left(\sigma_{\text{los}}(R_+^{(i)}) - \sigma_{\text{los}}(R_-^{(i)}) \right)^2}, \quad (10)$$

where $R_{\pm}^{(i)} \equiv R^{(i)} \pm \Delta R^{(i)}$. The basic assumption of a Gaussian likelihood function on the

binned velocity dispersions follows from the large kinematic sample measured for the galaxies here considered (hundreds of stars or more are spectroscopically resolved for MW classical satellites). Previous relevant studies on the subject adopted a similar Gaussian test statistic, see for instance [3, 43, 44]. According to equation (10), we also take into account in our analysis the uncertainty related to the data binning, as previously done in [36, 45].

The second important piece of information in our fitting procedure comes from the CDM concentration-mass relation, $R_{\max} = f(V_{\max})$ from equation (5). To exploit it, we assume a Gaussian test statistic of the form:

$$-2 \log \mathcal{L}_{\text{CDM}} = \left(\frac{\log_{10} R_{\max} - \log_{10} f(V_{\max})}{\sigma_{R_{\max}}} \right)^2, \quad (11)$$

where $\sigma_{R_{\max}} = 0.2$, as it follows from the discussion on CDM concentration-mass relation for MW dSphs adopted in this study. According to the same discussion, in our numerical analysis we penalize $R_{\max} - V_{\max}$ realizations which do not yield $V_c(r = 0.5 \text{ kpc}) > 19 \text{ km/s}$ and $25 \text{ km/s} < V_c(r = 10 \text{ kpc}) < 60 \text{ km/s}$, in which case we increase the test statistic of equation (11) by means of an additional exponential factor.

Based on the sum of equation (9) and equation (11), we have reported in figure 1 five different scenarios maximizing $\log \mathcal{L}_{\text{tot}}$: the SIDM model in the case of both constant and spatially varying stellar anisotropy, the CDM scenario with spatially dependent anisotropy, a cuspy and a cored DM halo model with constant orbital anisotropy and $\log \mathcal{L}_{\text{tot}} = \log \mathcal{L}_{\text{kin}}$. In order to offer to the reader a simple selection rule on what is the preferred model between the best-fit CDM and SIDM scenarios, in the same figure we have exploited the (asymptotic) notion of the Akaike Information Criterion [46], namely $\text{A.I.C.} \equiv 2\nu - 2 \log \mathcal{L}_{\text{tot}}$; ν represents the number of (independently adjusted) parameters of the model, respectively 6 and 7 for the CDM and the SIDM cases. By definition, the A.I.C. offers a trade-off between the goodness of the fit and the complexity of the model, characterized by ν . The preferred model within a set of candidates for the description of a given dataset is the one yielding the minimum A.I.C. value. Therefore, evaluating the difference $\Delta \text{A.I.C.} = \text{A.I.C.}_{\text{SIDM}} - \text{A.I.C.}_{\text{CDM}}$, we find an overall preference for SIDM as the selected model by dSph kinematic data in conjunction with the information extracted from pure CDM N-body simulations.

Eventually, the most important part of our statistical analysis consists in the Bayesian fit of the 7-parameter SIDM model on the basis of the $\log \mathcal{L}_{\text{tot}}$ discussed above. At the basis of the

adopted MCMC algorithm for the present study there is the affine-invariant ensemble sampler algorithm of [47]. We have used the public implementation of it within the package *emcee* discussed in some detail in [48]. Our Bayesian estimate of the SIDM parameters involves the initial assignment of log-flat priors as $-2 \leq \log_{10}(\sigma_0/[\text{km/s}]) \leq 2$, $-3 \leq \log_{10}(\rho_0/[\text{GeV}/\text{cm}^3]) \leq 3$, $-2.5 \leq \log_{10}(r_{1,\beta}/[\text{kpc}]) \leq 1.5$, while we flatly distribute $1 \leq \eta \leq 10$, $0 < 2^{\beta_0} \leq 1$, $0 < 2^{\beta_\infty} \leq 2$. Note that for the case of Sextans the posterior for β_∞ turns out to have two distinct modes, particularly correlated with r_1 distribution, also bimodal. We have focussed on the mode yielding $r_1 \leq 10^{1.5}$ kpc, restricting therefore to $0 < 2^{\beta_\infty} \leq 1$. This translates into a cut on large values for σ/m p.d.f., yielding for Sextans cross sections typically smaller than the ones probed by Fornax. For each galaxy we specifically set the *emcee* sampler to 280 walkers with 3300 steps and removed one third of the MCMC events as burn-in. We have checked for sampler convergence estimating both mean acceptance fraction and autocorrelation length for each of the fitted parameters.

Data availability. Data that support the plots within this paper and other findings of this study are available from the corresponding author upon reasonable request.

- [33] Geringer-Sameth A., Koushiappas S. M., & Walker, M. G. Dwarf galaxy annihilation and decay emission profiles for dark matter experiments. *Astrophys. J.* **801**, 74 (2015).
- [34] Plummer, H.C. On the problem of distribution in globular star clusters. *Mon. Not. R. Astron. Soc.* **71**, 460-470 (1911).
- [35] McConnachie, A. W. The observed properties of dwarf galaxies in and around the Local Group. *Astron. J.* **144**, 4 (2012).
- [36] Bonnivard, V., Combet, C., Maurin, D., & Walker, M. G. Spherical Jeans analysis for dark matter indirect detection in dwarf spheroidal galaxies - Impact of physical parameters and triaxiality. *Mon. Not. R. Astron. Soc.* **446**, 3002-3021 (2015).
- [37] An, J. H. & Evans, N. W. A Cusp Slope – Central Anisotropy Theorem *Astrophys. J.* **642**, 752-758 (2006).
- [38] An, J., Van Hese, E., & Baes, M. Phase-space consistency of stellar dynamical models determined by separable augmented densities. *Mon. Not. R. Astron. Soc.* **422**, 652-664 (2012).
- [39] Strigari, L. E., *et. al*, A common mass scale for satellite galaxies of the Milky Way. *Nature*

- 454**, 1096-1097 (2008).
- [40] Campbell, D. J. R., *et al.* Knowing the unknowns: uncertainties in simple estimators of galactic dynamical masses. *Mon. Not. R. Astron. Soc.* **469**, 2335-2360 (2017).
 - [41] González-Samaniego, A., *et al.*, Dwarf Galaxy Mass Estimators vs. Cosmological Simulations. *Mon. Not. R. Astron. Soc.* **472**, 4786-4796 (2017).
 - [42] Ullio, P. & Valli, M. A critical reassessment of particle Dark Matter limits from dwarf satellites. *J. Cosmol. Astropart. P.* **1607**, 025 (2016).
 - [43] Strigari, L. E., Koushiappas, S. M., Bullock, J. S., & Kaplinghat, M. Precise constraints on the dark matter content of Milky Way dwarf galaxies for gamma-ray experiments. *Phys. Rev. D* **75**, 083526 (2007).
 - [44] Charbonnier, C., *et al.* Dark matter profiles and annihilation in dwarf spheroidal galaxies: perspectives for present and future gamma-ray observatories - I. The classical dSphs. *Mon. Not. R. Astron. Soc.* **418**, 1526-1556 (2011).
 - [45] Bonnavard, V., *et al.* Dark matter annihilation and decay in dwarf spheroidal galaxies: The classical and ultrafaint dSphs. *Mon. Not. R. Astron. Soc.* **453**, 849-867 (2015).
 - [46] Akaike, H. A new look at the statistical model identification. *IEEE T. Automat. Contr.* **19**, 716-723 (1974).
 - [47] Goodman, J. & Weare, J. Ensemble samplers with affine invariance. *Comm. App. Math. Com. Sc.* **5**, 65-80 (2010).
 - [48] Foreman-Mackey, D., Hogg, D. W., Lang, D. & Goodman, J. emcee: The MCMC Hammer. *Publ. Astron. Soc. Pac.* **125**, 306 (2013)